RSC Advances

PAPER

View Article Online
View Journal | View Issue

Cite this: *RSC Adv.*, 2025, **15**, 20908

Atomic-level cation occupation and magnetic properties of Ce^{3+}-doped $ZnFe_2O_4$ spinel ferrite†

Xue Zeng, ‡[a] Jiaqian Liu,‡[b] Ke Chu, [a] Jie He, [c] Junwei Zhang,[d] Hanxing Zhu*[e] and Yong Peng *[d]

Received 3rd March 2025
Accepted 30th May 2025

DOI: 10.1039/d5ra01515d

rsc.li/rsc-advances

Rare-earth doping has been proven to be an effective strategy for tailoring the magnetic properties of ferrites. In this study, we report a direct experimental observation of the precise occupation of cations in Ce-doped spinel $ZnFe_2O_4$ ferrites. We demonstrate that divalent Zn^{2+} cations and trivalent Fe^{3+} cations respectively occupy all tetrahedral A sites and all octahedral B sites in $ZnFe_2O_4$ nanofibers, which aligns well with the normal spinel structure. Rare-earth Ce^{3+} ions preferentially occupy the octahedral sites of the $ZnFe_2O_4$ lattice, while the excess Fe^{3+} ions are displaced to the tetrahedral sites. The observed behavior is possibly due to the greater bond energy of Ce^{3+}–O^{2-} relative to Fe^{3+}–O^{2-}, requiring additional energy for Ce^{3+} to substitute into the B-sites. This cation redistribution leading to the appearance of 4f–3d orbital couplings results in the changes in magnetic performance at room temperature. With increasing Ce^{3+} doping concentration, the saturation magnetization (M_s) first increases before reaching a maximum and subsequently decreases. $ZnFe_2O_4$ nanofibers doped with 0.05 mmol Ce^{3+} exhibit the highest M_s value due to the enhanced A–O–B super-exchange interaction.

1. Introduction

Magnetic spinel ferrites, as strongly correlated electronic systems, have found extensive applications in new spintronic devices, microwave devices, biomedical, catalytic, and magnetic memory technologies.[1–7] The magnetic performance of spinel ferrites is highly dependent on specific ion occupancy and distribution. The structural changes with tunability of cation inversion can result in the modification of intrinsic magnetic properties of spinel ferrites, including Néel temperature, magnetization and other local magnetic properties. The cation occupancy can be influenced by the material preparation process, annealing temperature, and doping with magnetic or non-magnetic ions.[8,9] Rare-earth doping has been found to be a particularly effective strategy for significantly tailoring the magnetic properties of spinel ferrites. After rare-earth doping, the 4f orbitals totally screened by 5s and 5p orbitals of rare-earth elements couple with the 3d orbitals of transition group elements in ferrite, inducing more pronounced and complex correlations between electronic charges, spins, orbitals, lattices, magnetic moments, and magnetic domains. Previous studies have shown that the magnetic properties of ferrite nanomaterials can be modified by the incorporation of rare earth elements.[10–12] When high-spin transition metal ions were partially replaced by rare earth ions in ferrites, they exhibit enhanced spin–orbital (3d–4f) coupling and a systematic change in magnetic moments. This coupling stems from the progressive filling of electrons in the 4f shells, which not only modifies the structure but also alters the magnetic properties, such as magnetoelectric, magneto-optical, and other novel physical effects.[13–17] However, obtaining direct imaging evidence of rare-earth dopant sites and ion occupancy in ferrites has remained scarce.

Zinc ferrite ($ZnFe_2O_4$, ZFO), as an important member of the spinel family, has many potential applications as adsorbents,[18] catalysts,[19] gas sensors.[20] It exhibits a typical spinel structure (Fig. 1a and b), where 32 oxygen ions are closely packed, and 24 metallic cations are distributed across two crystallographic sites: the tetrahedral sites (A sites) and the octahedral sites (B sites). This distribution results in an antiparallel arrangement of magnetic moments in the two sub-lattices, with the net magnetic moments between these sub-lattices ultimately determining the unique magnetic properties of spinel ferrites.[21,22] It is well known that the structural, electrical, and magnetic properties of spinel ferrites are influenced by factors

[a]*School of Materials Science and Engineering, Lanzhou Jiaotong University, Lanzhou 730070, China*

[b]*School of Mathematics and Physics, Lanzhou Jiaotong University, Lanzhou 730070, China*

[c]*School of Chemistry and Chemical Engineering, Lanzhou Jiaotong University, Lanzhou 730070, China*

[d]*Electron Microscopy Centre of Lanzhou University, Key Laboratory of Magnetism and Magnetic Materials of the Ministry of Education, School of Materials and Energy, Lanzhou University, Lanzhou 730000, China. E-mail: pengy@lzu.edu.cn*

[e]*School of Engineering, Cardiff University, Cardiff CF24 3AA, UK. E-mail: ZhuH3@cardiff.ac.uk*

† Electronic supplementary information (ESI) available. See DOI: https://doi.org/10.1039/d5ra01515d

‡ Co-first authorship.

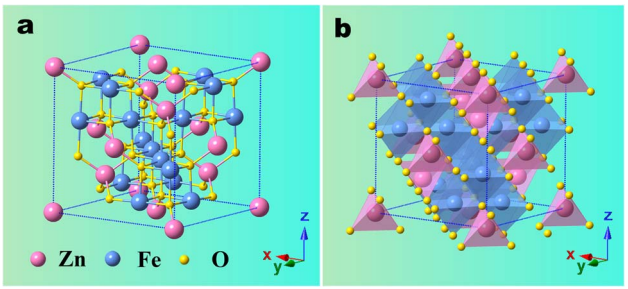

Fig. 1 The crystal structure and chemical composition of normal spinel ZFO and ZCFO ferries. (a) Ball-and-stick mode of normal spinel ZFO unit cell. The pink and blue spheres represent Zn cations and Fe cations, respectively, and O anions are in yellow. (b) Polyhedral model. Zn cations are located in tetrahedral A sites marked in pink. Fe cations are located in octahedral B sites marked in blue.

such as grain size, the specific substitution sites of doped ions, and annealing temperature. Therefore, selecting an appropriate synthesis method is particularly important. Spinel ferrites are typically prepared thorough sol–gel, hydrothermal, co-precipitation, and ball milling methods.[23,24] We prepared $ZnFe_2O_4$ ferrite nanofibers *via* electrospinning and regulated their structural and magnetic properties by doping with rare-earth elements. Numerous rare-earth ions have been doped into spinel ferrites to tailor their magnetic magnetoelectric properties. Mohd. Hashim *et al.*[25] reported the doping effects of Ce^{3+} and Dy^{3+} co-doped cobalt ferrites and found that the saturation magnetization M_s decreased and the coercivity H_c increased with the increase in co-dopant contents. Sagar E. Shirsath *et al.*[26] studied the structural and magnetic properties of Ce^{4+} doped $NiFe_2O_4$ ferrites and found that the saturation magnetization M_s and the Curie temperature T_c decreased with the increase in Ce^{4+} ions. K. Muthuraman *et al.*[27] investigated Ce^{3+}-doped $MgFe_2O_4$ ferrites prepared *via* sol–gel method. It revealed enhanced saturation magnetization (M_s) and coercivity with increasing Ce^{3+} content. In order to tailor the magnetic properties of $ZnFe_2O_4$ and diversify its applications, the rare-earth element Ce^{3+} is anticipated to be an effective method for tuning the magnetic properties of $ZnFe_2O_4$ spinel ferrites, owing to its large ionic radius (Ce^{3+} 1.03 Å, Ce^{4+} 0.92 Å), diverse electron configurations (Ce^{3+} and Ce^{4+}), and high magnetic moment (2.54 μ_B).[28–30] However, there is a notable absence of a comprehensive and accurate explanation regarding the precise occupation of rare-earth Ce atoms and the relationship between the preferred site of dopant Ce^{3+} ions and the magnetic properties of Ce-doped $ZnFe_2O_4$ ferrites. Consequently, it is essential to directly obtain accurate ion occupancy and long-range ordered distribution. Aberration-corrected transmission electron microscopy (Cs-corrected STEM) has been proven to enable direct observation of atomic structure and specific substitution positions of doped atoms due to its ultra-high spatial resolution.[31,32]

In this study, we performed direct observation of the preferred atomic sites of dopants and the occupation sites in Ce-doped $ZnFe_2O_4$ using aberration-corrected STEM (Cs-STEM). We systematically investigated the influences of doping Ce^{3+} on the morphology, cation distributions, and magnetic properties. Our work significantly contributes to tailoring the magnetic properties of rare-earth Ce-doped $ZnFe_2O_4$ ferrites, providing guiding principles for further improving their performance.

2. Experimental

2.1 Nanofiber synthesis

$ZnCe_xFe_{2-x}O_4$ ($x = 0$, 0.05, 0.1) nanofibers were synthesized *via* electrospinning. The preparation of a typical precursor solution involved two steps. In the first step, solution A was prepared, which included 1 mmol zinc nitrate, x mmol ($x = 0$, 0.05, 0.1) cerium nitrate, and $(1 - x)$ mmol iron nitrite nonahydrate, 2 mmol iron nitrite nonahydrate (A.R., Alfa-Aesar Inc., Ward Hill, NJ, USA), and 5 mL *N*,*N*-dimethyl formamide (DMF, A.R., Tianjin Chemical Corp., Tianjin, China). In the second step, 1 mL of solution A, 1 mL of ethanol, and 0.157 g of polyvinylpyrrolidone (PVP, $M_w \approx 1\,300\,000$, Alfa-Aesar Inc., Ward Hill, NJ, USA) were mixed in a 5 mL vessel and stirred for 6–8 hours. The electrospinning process was conducted at 18 kV DC voltage, with a 15 cm gap from the needle tip to the collector, and a feed rate of 0.4 mL h^{-1}. The annealing process consisted of initial heating at 200 °C for 2 hours, followed by heating at 850 °C for 3 hours, and cooling to room temperature at a rate of 1 °C min^{-1} in air.

2.2 Nanofiber characterization

The morphology, atomic-level crystal structure, and chemical composition of the individual single-particle-chain $ZnFe_2O_4$ (ZFO) and Ce-doped $ZnFe_2O_4$ (ZCFO) nanofibers were characterized using an aberration-corrected scanning transmission electron microscope (FEI Titan Cubed Themis G2 300, FEI, USA), which was equipped with an energy-dispersive X-ray (EDX) spectrometer (Bruker EDX, Bruker, USA) and operated at 300 kV. X-ray diffraction (XRD) analysis was performed using a Philips X'Pert Pro MPD instrument (Netherlands). The element states were detected by X-ray photoelectron spectroscopy (XPS, ESCALAB Xi+, Thermo Scientific). Magnetic properties were measured with a magnetic property measurement system (MPMS, SQUID-VSM, Quantum Design) and a superconducting quantum interference device (SQUID) magnetometer (MPMS XL-7, UK).

3. Results and discussion

Single-particle-chain $ZnFe_2O_4$ (ZFO) and Ce-doped $ZnFe_2O_4$ (ZCFO) nanofibers were successfully synthesized by electrospinning. Fig. 1a and b illustrate the theoretical unit-cell structure of a normal spinel ZFO ferrite, which contains a total of 56 ions. 8 divalent Zn^{2+} ions and 16 trivalent Fe^{3+} ions can be respectively distributed in the tetrahedral A sites and octahedral B sites (corresponding polyhedral sites shown in Fig. 1b). The Zn cations are marked as pink balls (atomic radius of 1.39 Å), and the Fe cations as blue balls (atomic radius of 1.27 Å), as shown in Fig. 1a. 32 O anions are closely packed to form

a cubic structure. Fig. 1b shows the corresponding polyhedral-shaped sites where the two types of atoms are located.

High-angle annular dark-field scanning transmission electron microscopy (HAADF-STEM) images confirm that individual ZFO and ZCFO are composed of single particles stacked along the nanofiber axis. All nanofibers exhibit a continuous structure with an almost uniform size of single particles, with an average diameter of approximately 85 nm, ranging from 75 nm to 95 nm (ESI Fig. S1†). The Zn, Fe, and O elements are evenly distributed throughout the nanofiber, indicating a uniform chemical phase (ESI Fig. S2†). Fig. 2 presents representative Rietveld refined XRD pattern of spinel $ZnCe_xFe_{2-x}O_4$ nanofibers (x = 0, 0.05, 0.1). The diffraction peaks indexed to (220), (311), (400), (422), (511), (440), (620), (533), (444), (642) and (553) planes verified the cubic FCC structure (space group: $Fd\bar{3}m$) of the $ZnCe_xFe_{2-x}O_4$ nanofibers. The structural parameters such as lattice parameters (Å), cell volume (Å^3) and cell density (g cm^{-3}) are tabulated in Table 1. As the doping amount increases, all diffraction peaks shift to lower angles. This shift suggests successful doping of Ce^{3+} cations into the interstitial sites by replacing some Fe^{3+} cations on the octahedral B sites, leading to an increase in the lattice constant, the volume and density of the unit cell as shown in Table 1. From the XRD refinement data, a small amount of secondary phases CeO_2 will be generated with increasing Ce^{3+} ions concentration. When the doping amount is 0.05 mmol and 0.1 mmol, the weight fraction of the CeO_2 impurity phase is 2.33% and 3.15%, respectively. Since Ce^{3+} has a larger ionic radius (1.03 Å) compared to Fe^{3+} (0.645 Å), the replacement is energetically unfavorable, leading to a distortion in the crystal symmetry. Additionally, excess Ce^{3+} ions that do not incorporate into the lattice accumulate at the grain boundaries, promoting the formation of CeO_2. The substitution process requires significant energy due to the longer Ce^{3+}–O^{2-} bond length relative to Fe^{3+}–O^{2-}, further driving the segregation of CeO_2 at the grain boundaries.

The atomic-level cation distributions of individual $ZnFe_2O_4$ (ZFO) nanoparticles were directly captured by Cs-STEM. Fig. 3a–c display experimental images of a ZFO particle projected from [001], [011], and [111] orientations, respectively. It should be noted that the contrast in HAADF-STEM images is sensitive to the atomic number Z (approximately proportional to $Z^{1.7}$). When atomic columns have a similar number of atoms, those with a higher atomic number Z exhibit greater contrast. However, if the atomic columns vary significantly in length, the contrast depends on the average atomic number and the number of atoms within the column. Fig. 1a demonstrates that Fe atomic columns in octahedral sites are distinctly brighter than the surrounding Zn atomic columns in tetrahedral sites, despite having the same length along the [001] orientation. Although Zn (Z = 30) has a slightly higher atomic number than Fe (Z = 26), the Fe atomic columns contain twice as many O atoms, enhancing the overall contrast of the octahedral sites. This aligns with the preference of Zn^{2+} ions for tetrahedral sites due to their sp^3 covalency. Additionally, Zn atoms, with a larger radius (1.39 Å) compared to Fe atoms (1.27 Å), occupy the tetrahedral A sites (marked by red circle 1), while Fe atoms occupy the octahedral B sites (marked by red circle 2). This observation strongly suggests that the ZFO ferrites have an ideal normal spinel structure, which is further confirmed by [011] and [111] oriented images.

The unit-cell models in Fig. 3g–i, with three crystal orientations, perfectly match the experimental Cs-STEM images, showing that all tetrahedral A sites are occupied by Zn cations and all octahedral B sites by Fe cations. Fig. 2d–f illustrate the line intensity profiles of '1', '2', and '3' marked by light blue frames, indicating pure Zn atomic columns at A sites, Fe atomic columns at B sites, and Zn–Fe mixed atomic columns, respectively. These profiles correspond well with the ion occupations in the 3D unit-cell models.

The specific substitution sites of the dopant Ce atoms in the $ZnFe_2O_4$ (ZCFO) nanofibers were imaged using Cs-STEM. Fig. 3a

Table 1 Structural parameters of $ZnCe_xFe_{2-x}O_4$ (x = 0, 0.05, 0.1) ferrites after Rietveld refinement

Ce content x	a (Å)	Volume (Å^3)	Density (g cm^{-3})	R_p	R_{wp}
0.00	8.44549	602.382	5.3228	7.05%	9.83%
0.05	8.45018	603.390	5.3432	10.31%	14.79%
0.1	8.45018	603.390	5.3432	8.96%	11.53%

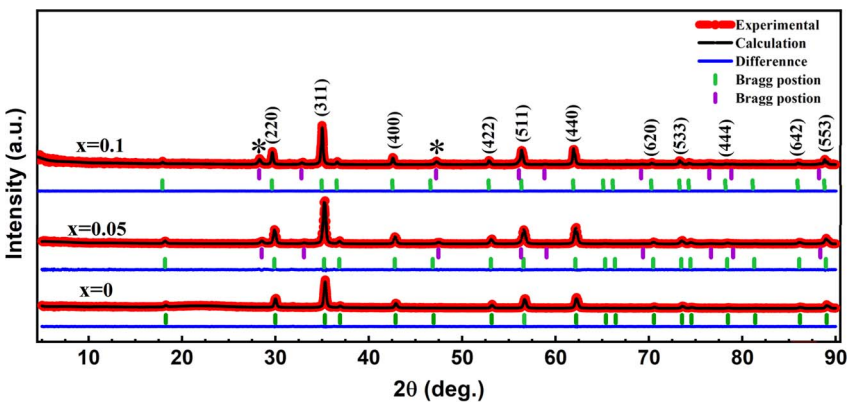

Fig. 2 Rietveld refined XRD pattern of the spinel $ZnCe_xFe_{2-x}O_4$ nanofibers (x = 0, 0.05, 0.1).

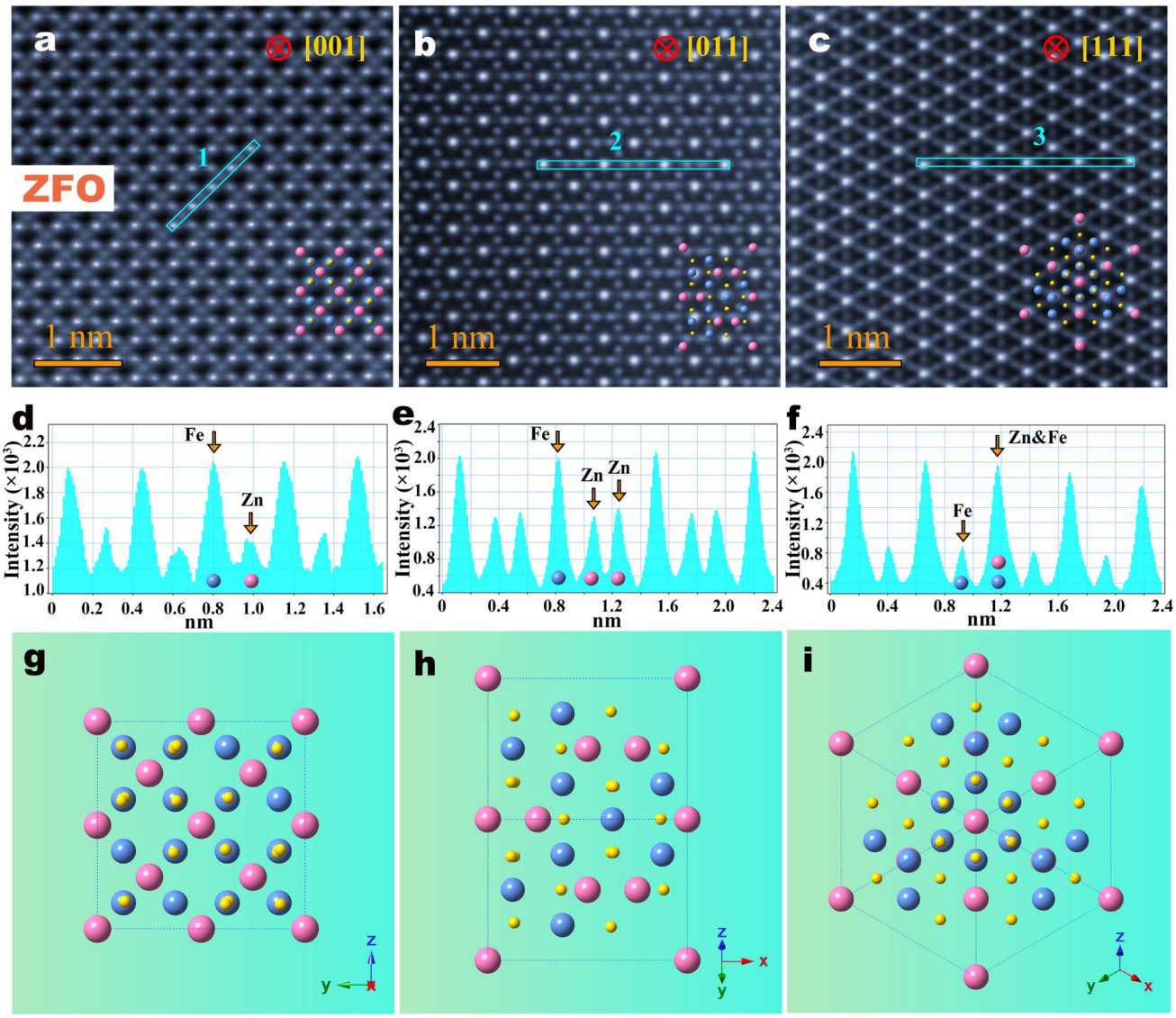

Fig. 3 Atomic-level ion distributions of normal spinel ZFO. (a–c) The Cs-STEM images of the individual ZFO nanoparticle observed along [001], [011] and [111] orientations, respectively. (d–f) Line intensity profiles for the atomic columns along blue frames '1', '2' and '3' in (a–c), respectively. (g–i) Perspective view of unit cells along [001], [011] and [111] orientations, respectively.

presents the Cs-STEM atomic image of the ZCFO nanofibers along the [001] orientation, revealing that the ZCFO nanofibers maintain the spinel crystal structure and that dopant Ce substitutions occur in the Fe atomic columns. Through contrast feedback in this atomic image, it can be observed that the brightness of atomic columns at tetrahedral A sites has significantly increased, and there is slight distortion of atoms at octahedral B sites, which are not ideal dots. This is attributed to the atomic number Z (58) of the Ce atom being significantly greater than the atomic number Z (26) of the Fe atom. Consequently, we infer that dopant Ce atoms randomly replace Fe atoms at octahedral B sites, causing distortion of atomic columns at B sites, while the displaced Fe atoms diffuse to tetrahedral A sites, contributing to the increase in atomic intensity at tetrahedral A sites. This can be demonstrated by the line intensity profile obtained from the blue rectangular box '1' as shown in Fig. 4d. If dopant Ce atoms were to replace Zn atoms in tetrahedral A sites, it would only lead to an increase in atomic strength in tetrahedral A sites, without causing atomic distortion in octahedral B sites. Here, our direct experimental observations have been unambiguously confirmed by Mössbauer spectroscopy measurements (ESI Fig. S3†), which provide definitive evidence that a fraction of Fe^{3+} ions are sterically driven into tetrahedral A sites. We further performed EDX atomic elemental mappings to verify the accurate sites of the substituted Ce ions. As shown in Fig. 4j–n, the images clearly reveal that the Ce cations only randomly substituted for the Fe cations at B sites rather than Zn cations. Cs-STEM images taken along the [011] and [111] orientations further verify our observations, as shown in Fig. 4b and c. The intensity profiles obtained from the blue rectangular boxes '2' and '3' of atomic columns further confirm the precise substitution sites of

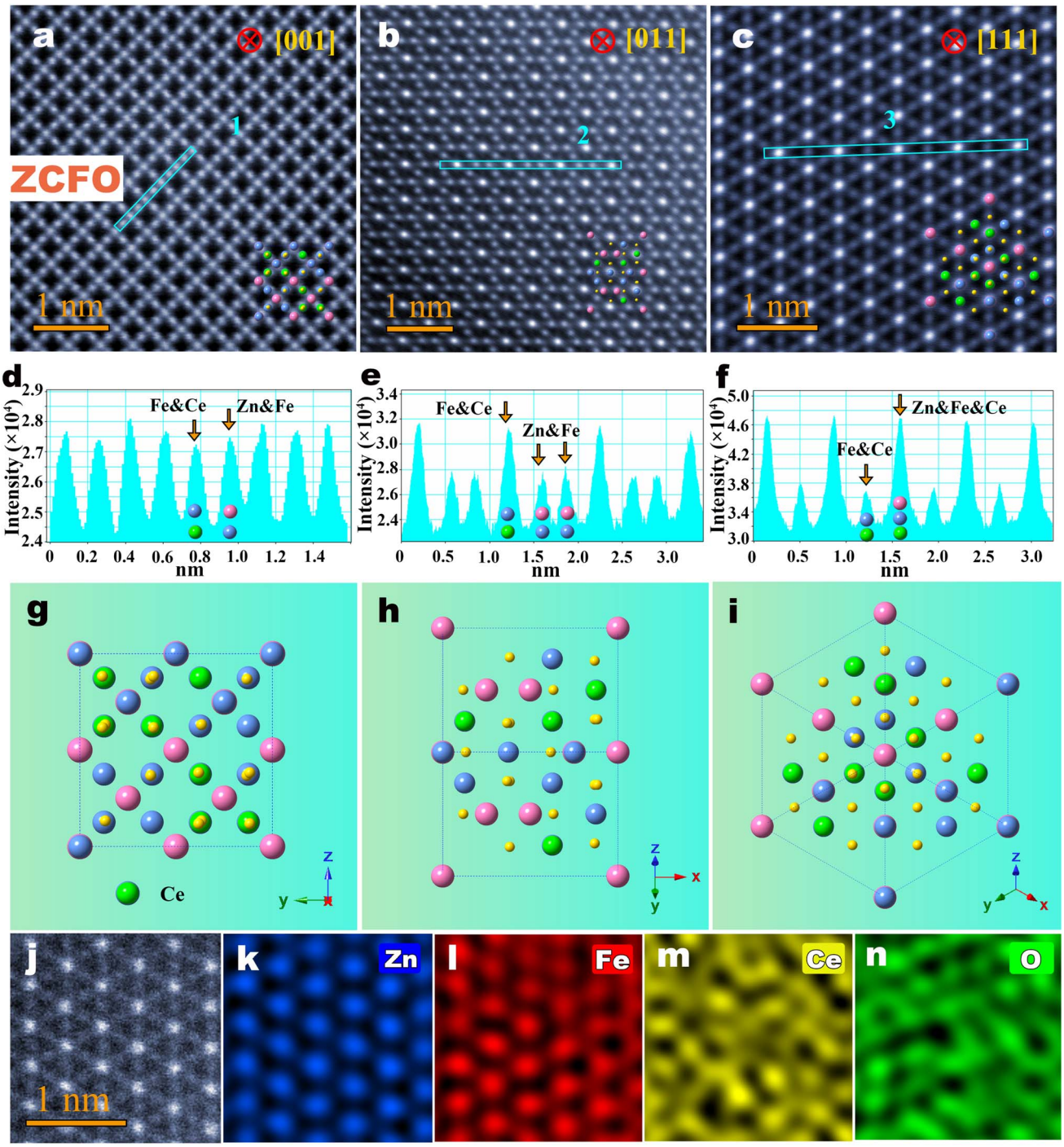

Fig. 4 Atomic-level ion distributions of Ce-doped normal spinel ZFO. (a–c) The Cs-STEM images of the individual ZCFO nanoparticle observed along [001], [011] and [111] orientations, respectively. (d–f) Line intensity profiles for the atomic columns along blue frames '1', '2' and '3' in (a–c), respectively. (g–i) Perspective view of unit cells along [001], [011] and [111] orientations, respectively. (j–n) Atomic resolution EDX elemental mappings of $ZC_{0.1}FO$ nanofiber along the [111] orientation, showing the exact distribution of Zn, Fe, Ce and O elements.

dopant Ce atoms, as can be seen in Fig. 4e and f, where pure Zn atomic columns have transformed into Zn–Fe mixed atomic columns, and pure Fe atomic columns have transformed into Fe–Ce mixed atomic columns. The corresponding atomic unit cell models shown in Fig. 4g–i, in which the green atoms represent the doping Ce atoms, match well with the direct observations of the ZCFO images.

To validate our direct experimental observations and confirm the successful incorporation of Ce ions into the ZFO nanofibers, the elemental states of ZFO and ZCFO nanofibers were detected by XPS technique as shown in Fig. 5a and b. For Fe 2p spectrum of ZFO and ZCFO nanofibers, the spin–orbit split components ($2p_{3/2}$ and $2p_{1/2}$) can be resolved into distinct spectral contributions from Fe^{3+} oxidation states. Relative to

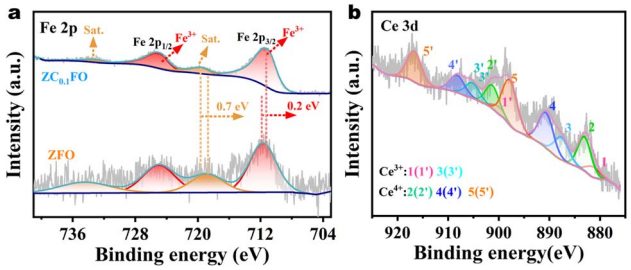

Fig. 5 XPS spectra of ZFO and ZCFO nanofibers: (a) Fe 2p; (b) Ce 3d

ZFO nanofibers, the Fe $2p_{3/2}$ peak in Ce-doped ZFO nanofibres exhibits a positive binding energy shift of 0.2 eV. Such shift of binding energy location for Fe $2p_{3/2}$ delivers the reduction behavior of high-valence Fe^{3+} with the interaction of Ce into $ZnFe_2O_4$ ferrites. Fig. 4b displays the Ce 3d XPS spectrum, where: (i) peaks at 881.85 eV and 904 eV are assigned to Ce^{3+} $3d_{5/2}$ and $3d_{3/2}$ and (ii) Ce^{4+} signal (~917 eV) is detected, confirming the coexistence of Ce^{3+} and Ce^{4+} oxidation state. The tetravalent Ce^{4+} ions predominantly exist as a secondary phase.

To explore the effect of Ce^{3+} doping on ZFO nanofibers and to deeply study the correlation between micro-structure and magnetic performance, the magnetic properties of the $ZnCe_xFe_{2-x}O_4$ nanofibers (x = 0, 0.05, 0.1) were measured using a PPMS and a SQUID magnetometer. External magnetic field dependences of magnetization for spinel $ZnCe_xFe_{2-x}O_4$ nanofibers (x = 0, 0.05, 0.1) were obtained in a 7 T magnetic field at the temperature of 300 K and 2 K as shown in Fig. 6a and b, respectively. From the hysteresis loops, it is found that the saturation magnetization (M_s) value and the M/H of the samples increase and then decrease with the increase of Ce^{3+} doping concentration in ZFO nanofibers, where $ZCe_{0.05}FO$ nanofibers exhibit the largest M_s and M/H values. Meanwhile, as the Ce doping content increases, the values of coercivity (H_c) and residual magnetization (M_r) approach zero, showing that all samples exhibit superparamagnetic behavior at 300 K. This is attributed to the small size of individual particles on the $ZnCe_xFe_{2-x}O_4$ nanofibers, which exhibit a single-domain state. From the hysteresis loops at 5 K, it is evident that the $ZnCe_xFe_{2-x}O_4$ nanofibers exhibit ferromagnetic behavior, including greater coercivity (H_c) of ~1250 Oe and residual magnetization (M_r). Fig. 6c–f show the temperature dependence of zero-field-cooled (ZFC) and field-cooled (FC) magnetization curves of the spinel $ZnCe_xFe_{2-x}O_4$ nanofibers (x = 0, 0.05, 0.1) measured at temperatures ranging from 2 K to 400 K with an applied magnetic field of 100 Oe. The ZFC/FC curves demonstrate a similar variation tendency with the change of temperature. As the temperature decreases from 400 K to 22 K, the ZFC/FC magnetization values of all nanofibers increase consistently, then decrease when the temperature is below the blocking temperature (T_B) 22 K. The ZFC and FC curves overlap below room temperature (300 K), indicating that the Curie temperature (T_c) of all the nanofibers is below 300 K, as shown in the insets of Fig. 6c–f. This suggests that the spinel $ZnCe_xFe_{2-x}O_4$

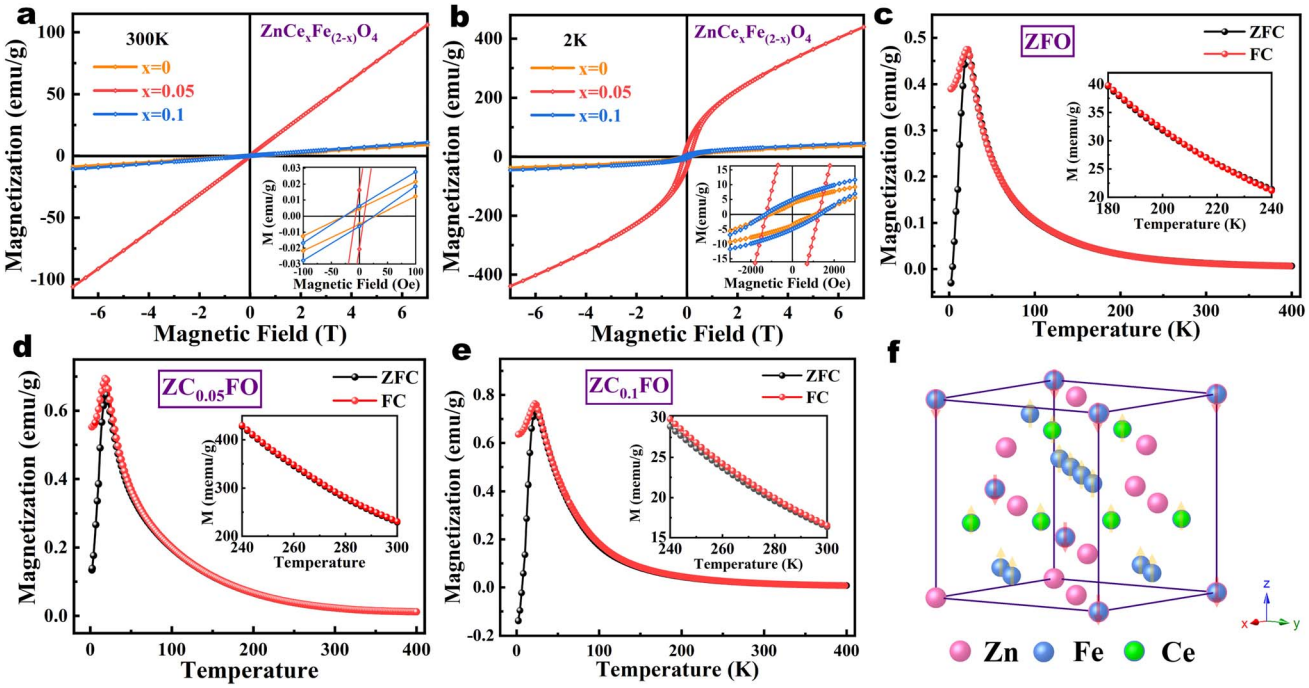

Fig. 6 Magnetic properties of the spinel $ZnCe_xFe_{2-x}O_4$ nanofibers (x = 0, 0.05, 0.1). (a) The typical hysteresis loops of $ZnCe_xFe_{2-x}O_4$ nanofibers (x = 0, 0.05, 0.1) measured under an external magnetic field of 7 T and a temperature of 300 K. (b) The typical hysteresis loops of $ZnCe_xFe_{2-x}O_4$ nanofibers (x = 0, 0.05, 0.1) measured under an external magnetic field of 7 T and a temperature of 2 K. (c–e) The typical ZFC/FC curves measured at a temperature ranging from 2 T to 400 T under an applied magnetic field of 100 Oe. Insets illustrate the magnification of curves near 300 K. (f) Schematic diagram of magnetic moment arrangement in ZCFO unit cell, with arrows representing the direction of magnetic moments, yellow arrows representing the magnetic moments of octahedral cations, and red arrows representing the magnetic moments of tetrahedral cations.

nanofibers ($x = 0$, 0.05, 0.1) exhibit superparamagnetic characteristics at room temperature, which is consistent with the hysteresis loop results.

The increase in magnetization (M_s) should be associated with the substitution of Fe^{3+} cations by Ce^{3+} cations, including the distribution of cations, canted spin structure, and super-exchange interactions between cations and O^{2-} anions. According to the direct observation of ion occupancy, the specific structural formula of ZCFO can be represented by $(ZnFe)^{A}[CeFe]_2^{B}O_4$, where the parentheses denote the A sites and the square brackets indicate the B sites. A schematic diagram of magnetic moment arrangement in ZCFO unit cell is shown in Fig. 6f. In this case, the net magnetization in spinel ferrites requires:[33]

$$M_{net} = \sum M_{oct.(B)} - \sum M_{oct.(A)}$$

where $\sum M_{oct.(B)}$ and $\sum M_{oct.(A)}$ represent the sum of the magnetic moments of magnetic cations located at the octahedral and tetrahedral sites. Among all cations, Zn ions are non-magnetic, the magnetic moments of Ce^{3+} and Fe^{3+} ions are 2.54 μ_B and 5 μ_B respectively. The magnetism in spinel ferrites is controlled by the super-exchange interactions magnetic cations mediated by O^{2-} ions between A and B sites. Among them, the interaction A–O–B (J_{AB}) is the strongest, B–O–B (J_{BB}) is weaker, and A–O–A (J_{AA}) is the weakest.[34] In normal spinel ZFO ferrites, there is only weak B–O–B interaction due to the non-magnetic Zn^{2+} cations at A sites. Here, due to the Fe^{3+} cations at B sites are replaced by the rare-earth Ce^{3+} cations and the excess Fe^{3+} cations occupying the A sites resulting in the strengthening of the magnetic linkages between Fe_A^{3+}–O–Fe_B^{3+} and Fe_A^{3+}–O–Ce_B^{3+}. The super-exchange interaction A–O–B is strengthened, resulting in an increase in saturation magnetization M_s of ZCFO ferrites. The presence of secondary phases CeO_2 along with $ZnFe_2O_4$ nanofibers when the doping amount is 0.1 mmol may cause a decrease in saturation magnetization M_s.

4 Conclusions

In summary, we demonstrated a direct observation of the distributions and occupation sites of the cations in the spinel Ce-doped $ZnFe_2O_4$ nanofibers using Cs-STEM. The atomic-level STEM images revealed that the ZFO nanofibers possess an ideal normal spinel structure. Combined with atomic-column resolution EDX elemental mappings, these images further directly proved that the doping rare-earth Ce^{3+} cations randomly substitute for the Fe^{3+} cations at the octahedral sites, while excessive Fe^{3+} cations occupy the tetrahedral sites. This substitution leads to the varied magnetization of the Ce-doped ZFO ferrites. Magnetic measurements indicate that the $ZnCe_xFe_{2-x}O_4$ nanofibers ($x = 0$, 0.05, 0.1) always maintain a superparamagnetic state, and the saturation magnetization (M_s) values first increase and then decrease with increasing Ce^{3+} content. The substitution of Fe^{3+} ions by rare-earth Ce^{3+} ions in Ce-doped ZFO ferrites results in a system with improved magnetic characteristics due to the enhanced A–O–B super-exchange interaction. Our results open the door for tailoring the magnetic properties of $ZnFe_2O_4$ ferrites by doping the rare-earth Ce^{3+} ions which may eventually be helpful for diversifying the applications of ferrite materials.

Data availability

The data supporting the findings of this study are available within the article and its ESI.† Additional datasets generated and analyzed during the current study are available from the corresponding author upon reasonable request.

Conflicts of interest

The authors declare no conflict of interest.

Acknowledgements

This work was supported by the National Natural Science Foundation of China (52101224, 12374011 and 51771085), the National Natural Science Foundation of Gansu (25JRRA954 and 24JRRA232) and National Key Research and Development Program of China (2022YFC2903504). This work is also supported by the Fundamental Research Funds for the Central Universities (lzujbky-2024-eyt01).

References

1 G. Hu and Y. Suzuki, Negative Spin Polarization of Fe3O4 in Magnetite/Manganite-Based Junctions, *Phys. Rev. Lett.*, 2002, **89**, 276601.
2 H. Zheng, J. Wanget, S. E. Lofland, Z. Ma, Z. Mohaddes-Ardabili, T. Zhao, L. Salamanca-Ribaal, S. R. Shinde, S. B. Ogale, F. Bai, D. Viehland, Y. Jia, D. G. Schlom, M. Wuttig, A. Roytburd and R. Ramesh, *Science*, 2004, **303**, 661–663.
3 C. Schmitz-Antoniak, D. Schmitz, P. Borisov, F. M. F. Groot, S. Stienen, A. Warland, B. Krumme, R. Feyerherm, E. Dudzik, W. Kleemann and H. Wende, *Nat. Commun.*, 2013, **4**, 2051.
4 T. P. Almeida, T. Kasama, A. R. Muxworthy, W. Williams, L. Nagy, T. W. Hansen, P. D. Brown and R. E. Dunin-Borkowski, Visualized Effect of Oxidation on Magnetic Recording Fidelity in Pseudo-Single-Domain Magnetite Particles, *Nat. Commun.*, 2014, **5**, 5154.
5 L. M. B. Alldredge, R. V. Chopdekar, B. B. Nelson-Cheeseman and Y. Suzuki, Spin-Polarized Conduction in Oxide Magnetic Tunnel Junctions with Magnetic and Nonmagnetic Insulating Barrier Layers, *Appl. Phys. Lett.*, 2006, **89**, 182504.
6 H. Zhong, X. Xiao, S. Zheng, W. Zhang, M. Ding, H. Jiang, L. Huang and J. Kang, Mass Spectrometric Analysis of Mono- and MultiPhosphopeptides by Selective Binding with $NiZnFe_2O_4$ Magnetic Nanoparticles, *Nat. Commun.*, 2013, **4**, 1656.
7 C. S. S. R. Kumar and F. Mohammad, Magnetic Nanomaterials for Hyperthermia-Based Therapy and Controlled Drug Delivery, *Adv. Drug Delivery Rev.*, 2011, **63**, 789–808.
8 R. Verma, F. Mazaleyrat, U. P. Deshpande and S. N. Kane, Ni Addition Induced Modification of Structural, Magnetic

Properties and Bandgap of Ni-Zn Nano Ferrites, *Mater. Today Chem.*, 2020, **32**, 329–333.

9 M. A. Almessiere, S. Güner, Y. Slimani, A. Baykal, S. E. Shirsath, A. D. Korkmaz, R. Badar and A. Manikandan, Investigation on the Structural, Optical, and Magnetic Features of Dy^{3+} and Y^{3+} Co-Doped $Mn_{0.5}Zn_{0.5}Fe_2O_4$ Spinel Ferrite Nanoparticles, *J. Mol. Struct.*, 2022, **1248**, 131412.

10 M. AsifIqbal, M. U. Irlam, I. Ali, M. Azhar Khan, M. R. Shahid, M. Hassan Khan and M. Khalid Mehmood, Study of physical, magnetic and electrical properties of rare-earth substituted Li-Mg ferrites, *J. Alloys Compd.*, 2017, **692**, 322–331.

11 V. C. Pujari, P. D. Mhase, S. M. Patange, P. S. More, S. S. Meena, S. F. Shaikh, A. M. Al-Enizi and S. S. Jadhav, Influence of Dy^{3+} doping on Mossbauer, ¨ magnetic and microwave absorption properties of M-type $Ba_{0.5}Ca_{0.5}Dy_xFe_{12-x}O_{19}$ hexaferrites, *J. Magn. Magn. Mater.*, 2024, **610**, 172555.

12 V. C. Pujari, P. D. Mhase, R. M. Mahindrakar, S. S. Meena, S. R. Kamble, S. M. Patange and S. S. Jadhav, Modifications in structure dependent magnetic parameters of Nd-doped Ba–Ca hexaferrites synthesized by sol gel using lemon extract as a fuel, *Ceram. Int.*, 2023, **49**, 40466–40477.

13 H. B. Vasili, B. Casals, R. Cichelero, F. Macià, J. Geshev, P. Gargiani, M. Valvidares, J. Herrero-Martin, E. Pellegrin, J. Fontcuberta and G. Herranz, Direct observation of multivalent states and 4f→3d charge transfer in Ce-doped yttrium iron garnet thin films, *Phys. Rev. B*, 2017, **96**, 014433.

14 N. Rezlescu and E. Rezlescu, The influence of Fe substitutions by R ions in a Ni Zn Ferrite, *Solid State Commun.*, 1993, **88**, 139.

15 S. E. Jacobo, S. Duhalde and H. R. Bertorello, Rare earth influence on the structure and magnetic properties of NiZn ferrites, *J. Magn. Magn. Mater.*, 2004, **2253**, 272–276.

16 G. V. Bazuev, O. I. Gyrdasova, S. I. Novikov and A. Y. Kuznetsov, Synthesis, structure, and magnetic properties of rare-earth-doped $Ni_{0.75}Zn_{0.25}Fe_2O_4$ nickel zinc ferrite, *Inorg. Mater.*, 2016, **52**, 932–938.

17 B. Zheng, J. Fan, B. Chen, X. Qin, J. Wang, F. Wang, R. Deng and X. Liu, Rare-earth doping in nanostructured inorganic materials, *Chem. Rev.*, 2022, **122**, 5519–5603.

18 F. Tomas-Alonso and J. M. P. Latasa, Synthesis and surface properties of zinc ferrite species in supported sorbents for coal gas desulphurisation, *Fuel Process. Technol.*, 2004, **86**, 191–203.

19 H. Lee, J. C. Jung, H. Kim, Y. M. Chung, T. J. Kim, S. J. Lee, S. H. Oh, Y. S. Kim and I. K. Song, Effect of pH in the preparation of $ZnFe_2O_4$ for oxidative dehydrogenation of *n*-butene to 1,3-butadiene: correlation between catalytic performance and surface acidity of $ZnFe_2O_4$, *Catal. Commun.*, 2008, **9**, 1137–1142.

20 G. Zhang, C. Li, F. Cheng and J. Chen, $ZnFe_2O_4$ tubes: synthesis and application to gas sensors with high sensitivity and low-energy consumption, *Sens. Actuators, B*, 2007, **120**, 403–410.

21 D. A. Vinnik, V. E. Zhivulin, D. P. Sherstyuk, A. Y. Starikov, P. A. Zezyulina, S. A. Gudkova, D. A. Zherebtsov, K. N. Rozanov, S. V. Trukhanov and K. A. Astapovich, Ni Substitution Effect on the Structure, Magnetization, Resistivity and Permeability of Zinc Ferrites, *J. Mater. Chem. C*, 2021, **9**, 5425–5436.

22 K. Nadeem, S. Rahman and M. Mumtaz, Effect of annealing on properties of Mg doped Zn-ferrite nanoparticles, *Mater. Int.*, 2015, **25**, 111–116.

23 S. E. Shirsath, D. Wang, S. S. Jadhav, M. L. Mane and S. Li, Ferrites Obtained by Sol-Gel Method, *Handb. Sol-Gel Sci. Technol.*, 2018, **25**, 696–732.

24 Y. Slimani, A. Baykal and A. Manikandan, Effect of Cr^{3+} substitution on AC susceptibility of Ba hexaferrite nanoparticles, *J. Magn. Magn. Mater.*, 2018, **458**, 204–212.

25 M. Hashim, M. Raghasudha, S. S. Meena, J. Shah, S. E. Shirsath, S. Kumar, D. Ravinder, P. Bhatt, A. R. Kumar and R. K. Kotnala, Influence of rare earth ion doping (Ce and Dy) on electrical and magnetic properties of cobalt ferrites, *J. Magn. Magn. Mater.*, 2018, **449**, 319–327.

26 S. E. Shirsath, S. S. Jadhav, B. G. Toksha, S. M. Patange and K. M. Jadhav, Influence of Ce^{4+} ions on the structural and magnetic properties of $NiFe_2O_4$, *J. Appl. Phys.*, 2011, **110**, 013914.

27 K. Muthuraman, V. Naidu, S. K. A. Ahmed and T. Vasudevan, Study of electrical and magnetic properties of cerium doped nano smart magnesium ferrite material, *Int. J. Comput. Appl.*, 2013, **23**, 65.

28 J. Xia, H. Zhao, B. Huang, L. Xu, M. Luo, J. Wang, F. Luo, Y. Du and C. Yan, Efficient optimization of electron/oxygen pathway by constructing ceria/hydroxide interface for highly active oxygen evolution reaction, *Adv. Funct. Mater.*, 2020, **30**, 1908367.

29 B. Yuan, X. Liu, X. Cai, X. Fang, J. Liu, M. Wu and Q. Zhu, Preparation of zinc and cerium or both doped Cu_2O photoelectric material *via* hydrothermal method, *Sol. Energy*, 2020, **196**, 74–79.

30 C. Jayachandraiah and G. Krishnaiah, Influence of cerium dopant on magnetic and dielectric properties of ZnO nanoparticles, *J. Mater. Sci.*, 2017, **52**, 7058–7066.

31 L. H. Bao, J. F. Zang, G. F. Wang and X. D. Li, Atomic-scale imaging of cation ordering in inverse spinel Zn_2SnO_4 nanowires, *Nano Lett.*, 2014, **14**, 6505–6509.

32 **https://en.wikipedia.org/wiki/Transmission_electron_microscopy**.

33 R. S. Yadav, J. Havlica, J. Masilko, L. Kalina, M. Hajduchová, V. Enev, J. Wasserbauer, I. Kuritka and Z. Kozakova, Structural, Cation Distribution, and Magnetic Properties of $CoFe_2O_4$ Spinel Ferrite Nanoparticles Synthesized Using a Starch-Assisted Sol−Gel Auto-Combustion Method, *J. Supercond. Novel Magn.*, 2015, **28**, 1851–1861.

34 R. S. Yadav, J. Havlica, J. Masilko, L. Kalina, M. Hajduchova, V. Enev, V. Wasserbauer, I. Kuritka and Z. Kozakova, Structural, cation distribution, and magnetic properties of $CoFe_2O_4$ spinel ferrite nanoparticles synthesized using a starch-assisted sol-gel auto-combustion method, *J. Supercond. Novel Magn.*, 2015, **28**, 1851–1861.